

# Hanbury Brown and Twiss measurements in curved space

Vincent H. Schultheiss<sup>1</sup>, Sascha Batz<sup>1</sup> and Ulf Peschel<sup>1,2\*</sup>

**When Hanbury Brown and Twiss (HBT) proposed their technique of intensity correlation measurements<sup>1–3</sup> to examine the angular size of stars in the visible range, they challenged the common conception of quantum mechanics and kicked off a discussion that led to the establishment of quantum optics<sup>4–6</sup>. In this Letter we revisit this fundamental technique and study its implications in the presence of space curvature. To this end we theoretically and experimentally investigate the evolution of speckle patterns propagating along two-dimensional surfaces of constant positive and negative Gaussian curvature, defying the notion that light always gains spatial coherence during free-space propagation. We also discuss the measurability of the traversed space's curvature utilizing HBT from an inhabitant's point of view. Through their symmetry, surfaces with constant Gaussian curvature act as analogue models for universes possessing non-vanishing cosmological constants.**

Since its origin as an astronomical method to reveal the spatial structure of stars light years away<sup>2,3</sup> the HBT-type intensity correlation technique has remained popular in astrophysics<sup>7,8</sup>, but has also proven to be a versatile lab tool in other fields of science such as condensed matter<sup>9–12</sup> and nuclear physics<sup>13–15</sup>. Only recently has the impact of particle interaction on HBT measurements been investigated in optical analogue systems<sup>16</sup>. It was shown that nonlinearity may have a considerable impact on the generated results, but might also provide new insight when taken into account. Similar effects may be anticipated for space curvature, the influence of which we are going to study in this Letter.

As predicted by general relativity, space is curved in principle and the consequences are tremendous when considered on cosmological scales. But the underlying effects are rather weak and their influence on optical measurements can thus be difficult to study in the laboratory. Therefore, to amplify space-curvature-related optical phenomena we abandon one spatial dimension and confine light propagation to the two-dimensional (2D) surface of appropriately shaped bodies. Wave propagation on macroscopic surfaces is entirely determined<sup>17,18</sup> by the intrinsic or Gaussian curvature  $K$ , defined as the inverse product of the two principal radii of curvature (Fig. 1). Here we focus on the case of constant  $K$ , as those systems maintain translational and rotational symmetry similar to the homogeneous and isotropic space surrounding us. In this Letter we exemplarily conduct HBT measurements on the surface of a sphere (with constant positive Gaussian curvature) and an hourglass-type figure (with constant negative Gaussian curvature), because these bodies of rotation can easily be manufactured with high accuracy out of crown glass (Fig. 2). Wave propagation is confined to the surface of the 3D bodies either by total internal reflection in the case of the sphere or by an index-step waveguide in the case of the hourglass figure. This approach is different from transformation optics, which employs an analogy between coordinate transformations and refractive index variations in the covariant formulation of Maxwell's equations, thus enabling the investigation of curvature-like

effects on a flat sheet<sup>19–22</sup>, but at the same time inherently foiling the system's rotational and translational invariance.

To understand the influence of intrinsic curvature on HBT measurements and speckle patterns let us first recall the latter phenomenon, which is a common by-product of coherent illumination. If a laser beam is reflected from a rough surface, a spatially random phase shift is imprinted onto the wave front. At an observation plane some distance  $z$  away from the surface the cumulative interference of the multitude of wave components from different directions and with random phases results in a grainy intensity pattern, called speckles. In flat space their size  $\rho$  can be estimated by calculating the fringe spacing of the interference pattern originating from two waves emitted from opposite edges of the illuminated area by<sup>23</sup>

$$\rho(z) \propto \frac{\lambda}{w_0} z \quad (1)$$

where  $\lambda$  is the wavelength of light and  $w_0$  the diameter of the illuminated area, that is of the spatially incoherent light source. The same approximation holds for speckle patterns originating from stars. Light emitted from two adjacent points on their surface is completely uncorrelated in phase, but as it propagates through empty space spatial correlations build up leading to a finite transverse correlation length when observed on Earth, which can be attributed to the star's angular size by virtue of equation (1). This is the scheme deployed by HBT<sup>2</sup>. Respective experiments involve determining the correlation length by measuring the second-order degree of coherence (DOC) function along a baseline in the transverse  $x$  direction:

$$g^{(2)}(x_1, x_2) = \frac{\langle I(x_1)I(x_2) \rangle}{\langle I(x_1) \rangle \langle I(x_2) \rangle} \quad (2)$$

Here  $\langle \cdot \rangle$  denotes taking the ensemble average (equivalent to temporal averaging), which we realize in our table-top experiment by randomly varying the phase structure of the incident light by means of a phase modulator. In contrast to astronomical observations we can track the whole evolution of the correlation length by imaging the stray light of the intensity distribution propagating along the surfaces of the glass figures on a CCD camera chip (Fig. 2).

Calling on a Gaussian Schell model<sup>24,25</sup> for the mutual intensity to mimic a Gaussian beam with random phase shifts and finite correlation length,  $g^{(2)}$  after some propagation distance  $z$  can be calculated from convoluting the initial mutual intensity with the point spread function of curved space (for a detailed derivation see the Supplementary Information). In the paraxial approximation it maintains its general form throughout propagation as

$$g^{(2)}(\Delta x, z) = 1 + e^{-\frac{\Delta x^2}{\rho(z)^2}} \quad (3)$$

<sup>1</sup>Institute of Optics, Information and Photonics, Friedrich-Alexander University Erlangen-Nürnberg (FAU), Haberstr. 9a, Erlangen 91058, Germany. <sup>2</sup>Institute of Condensed Matter Theory and Solid State Optics, Friedrich-Schiller-University Jena, Max-Wien-Platz 1, Jena 07743, Germany. \*e-mail: [ulf.peschel@uni-jena.de](mailto:ulf.peschel@uni-jena.de)

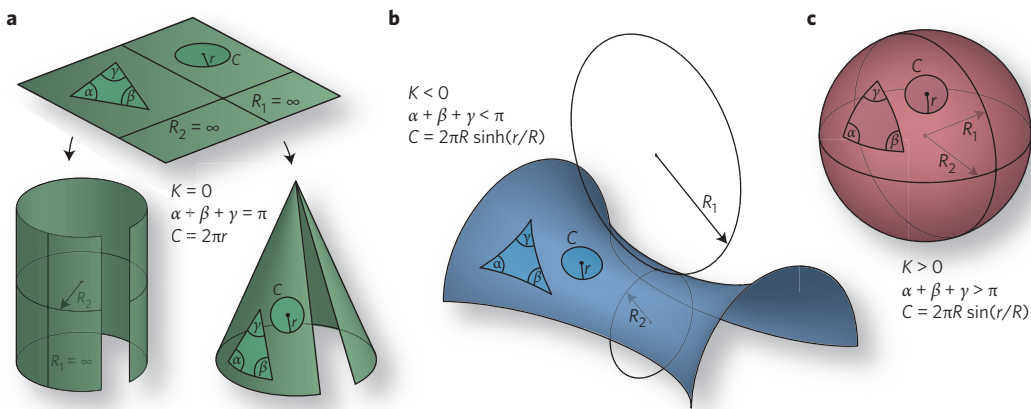


**Figure 1 | Collection of surfaces with constant Gaussian curvature  $K$ .** The Gaussian curvature is defined as the inverse product of the two principal radii of curvature  $R_{1,2}$  and is independent of the embedding in 3D space. Here we make use of the mean radius of curvature  $R = 1/\sqrt{|K|}$ . The sum of the interior angles of a triangle on a curved surface depends on both the Gaussian curvature and the enclosed area and in general is different from  $\pi$ . The circumference  $C$  of a circle depends on the radius  $r$  in a nontrivial way as shown. **a**, Different variations of a surface with zero Gaussian curvature realized by folding a flat sheet. **b**, Negatively curved saddle shape. Note that the radii  $R_{1,2}$  are assigned different signs when their respective centres are on opposite sides of the surface. **c**, Positively curved sphere with radius  $R_1 = R_2 = R$ .

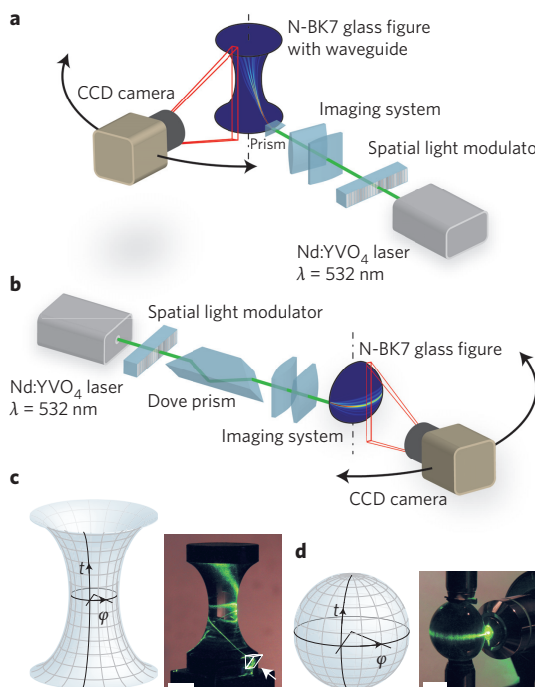


**Figure 2 | Experimental set-up.** **a**, Hourglass-type figure. The phase modulated Gaussian envelope field distribution at the back side of a linear spatial light modulator is imaged onto the coupling facet of a waveguide spanning along the surface of the glass figure. A prism is utilized to optimize the front coupling. A CCD camera is moved about the figure's axis of symmetry collecting column-wise images along the azimuthal angle. **b**, Half-sphere. The whole field distribution is rotated by a dove prism and then imaged onto the entrance face of the half-sphere. Inside the half-sphere the light is guided by total internal reflection. **c,d**, Coordinate systems as used to obtain the raw data depicted in the first column of Fig. 3. Images are taken stepwise along the azimuthal angle  $\varphi$ , and then rectified to vertically appear in the proper distance  $t$  along the figures' profile curves (with  $t = 0$  at the bodies' waists). Exemplary images of actual Gaussian beam propagation as seen in the experiment are depicted aside. Scale bars, 1 cm. **c**, The laser beam is coupled into the waveguide on the bottom right (the aiding prism is indicated by the white outline), winds around the figure's waist and hits the upper facet after slightly more than one turn. **d**, Coupling to the half-sphere with a microscope objective.

where  $\Delta x = x_2 - x_1$  and  $z$  are the geodesic lengths along the transverse  $x$  direction and the propagation direction, respectively (Fig. 3). The evolution of the correlation length  $\rho(z)$  is governed by its initial value  $\rho_0 = \rho(z = 0)$ , the field width  $w_0$  of the source and the mean radius of curvature  $R = 1/\sqrt{|K|}$ . Utilizing the Rayleigh length  $z_R = \pi w_0^2 n_{\text{eff}} / \lambda$  we define the speckle diffraction length  $z_S = z_R / \sqrt{1 + (w_0^2 / \rho_0^2)}$ , which in the limit of flat space is the propagation length after which the ensemble averaged transverse speckle size  $\rho$  has increased by a factor of  $\sqrt{2}$ . We obtain

$$\rho_{K<0}(z) = \rho_0 \sqrt{1 + \left(1 + \frac{R^2}{z_S^2}\right) \sinh^2\left(\frac{z}{R}\right)} \quad (4)$$

for negatively and

$$\rho_{K>0}(z) = \rho_0 \sqrt{1 - \left(1 - \frac{R^2}{z_S^2}\right) \sin^2\left(\frac{z}{R}\right)} \quad (5)$$

for positively curved surfaces. The limiting case of flat space with constantly growing transverse correlation length is achieved in both cases as  $R$  approaches infinity. Equations (4) and (5) are formally equivalent to the evolution of the width of a Gaussian beam propagating along a curved surface<sup>17</sup> provided that  $z_S$  is exchanged for  $z_R$ .

Both the experiments displayed in Fig. 3 and *ab initio* modelling depicted in Fig. 4 reproduce equations (4) and (5) surprisingly well. For light propagating along the negatively curved surface coherence builds up exponentially and, thus, even faster than in flat space (Fig. 3a–c and Fig. 4a). This is closely related to the evolution of the period of interference fringes behind a double slit<sup>18</sup>. In contrast, coherence properties of light propagating on positively curved surfaces display an oscillatory behaviour. The oscillation of the correlation length is contrary to the common conception of a strict gain of coherence during free-space propagation. Its amplitude and phase depend on the ratio between the sphere's radius of curvature and the speckle diffraction length. For  $z_S < R$  (Figs 3d–f and 4b) the correlation length initially increases until it reaches a maximum at  $z = \pi R/2$ , only to decline again to its initial value at  $z = \pi R$  and so on. Hence, the self-imaging properties of surfaces with constant positive Gaussian curvature as known, for example, from Maxwell's fish-eye lens<sup>26</sup> are also inherent to the dynamics of spatial correlations. For  $z_S > R$  the trend is shifted by  $\pi R/2$ , starting with a decrease of

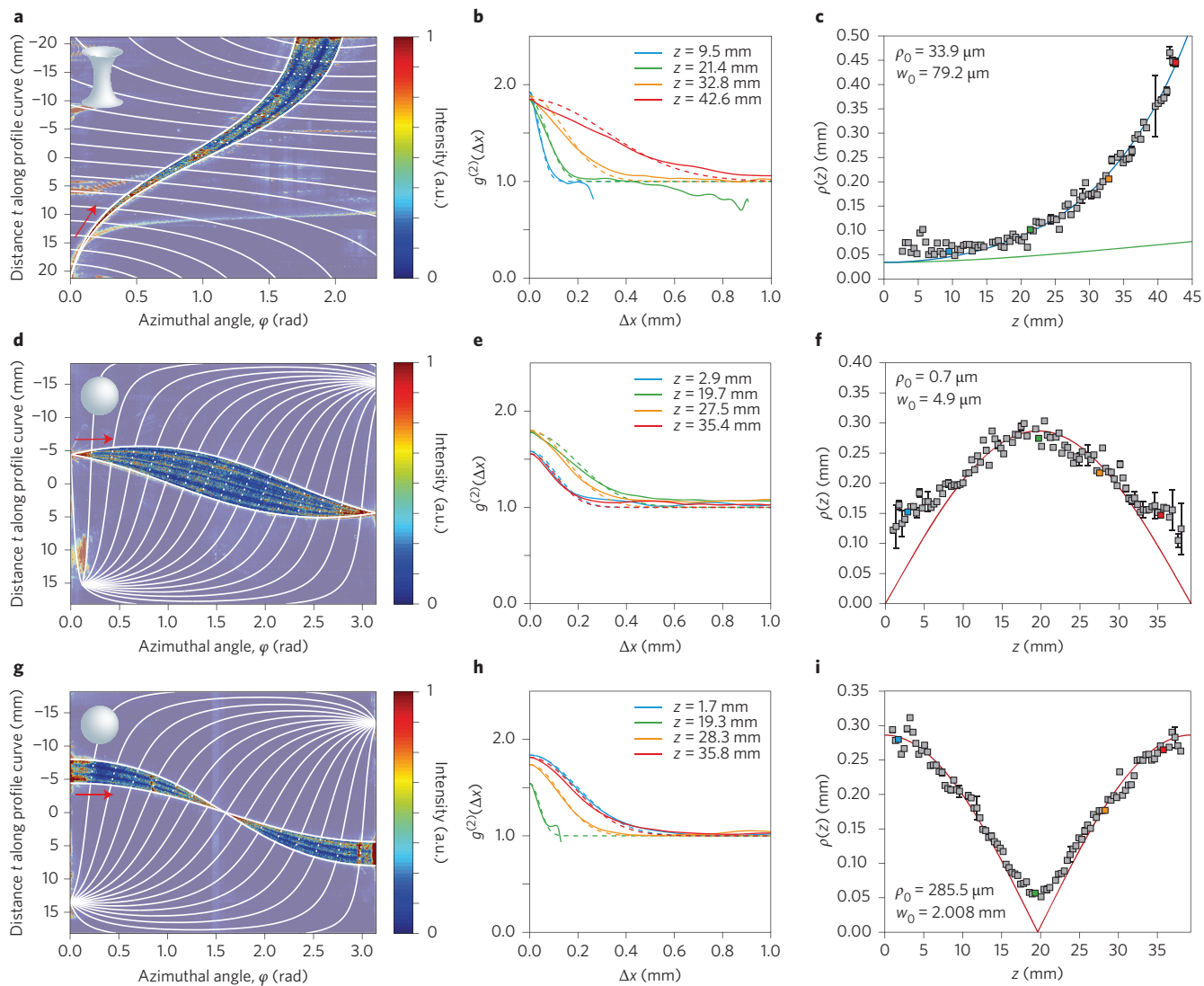


**Figure 3 | Experimental measurements of the second-order DOC function.** **a,d,g**, Realization of speckle evolution along the hourglass (**a**) and along the sphere for  $z_s < R$  (**d**) and  $z_s > R$  (**g**). The beams are coupled into the surfaces on the left and propagate to the right (indicated by red arrows). For the evaluation only a central region is considered (framing white lines). Geodesics running perpendicular to the propagation direction  $z$  are represented by white lines. In the vicinity of the beam's centre these lines correspond to the transverse  $x$  direction as used in the central subfigure column. Additional light spots are caused by reflections or parasitic beams running through the bulk of the figure. **b,e,h**, Second-order DOC function  $g^{(2)}(\Delta x)$  depending on the proper shift  $\Delta x$  in the transverse direction for four different propagation distances (corresponding to the coloured squares in **c,f** and **i**). Solid lines are measurements, dashed lines represent Gaussian fits. **c,f,i**, Correlation length  $\rho$  as obtained from Gaussian fits to  $g^{(2)}(\Delta x, z)$ . Error bars are confidence intervals of the fits. For small correlation lengths, deviations from theory are due to the limited experimental resolution caused by the finite scatterer and CCD pixel size. **c**, The solid blue line is a fit with equation (4), the solid green line is a comparison with zero Gaussian curvature for identical initial values. **f,i**, Solid red lines are fits with equation (5).

the correlation length. Still, the initial value is replicated at multiples of  $z = \pi R$  (Figs 3g–i and 4c). For an intermediate value  $z_s = R$  statistical features like the correlation length  $\rho(z)$  and the mean envelope field width  $w(z)$  remain unchanged during propagation. Owing to the finite scatterer size we could not resolve this static case experimentally, but simulations clearly show its existence (Fig. 4d).

As evident from our analysis, the evolution of the correlation length and consequently HBT measurements are tremendously influenced by space curvature, but the light source's actual size can still be ascertained, if the initial correlation length and the intrinsic curvature are known. However, also knowledge of  $z$  is required, which in most cases might not be directly available. Although in our experiment we can readily determine it from outside the surface, it is worthwhile to consider the standpoint of an inhabitant living inside the curved space, much like in astronomy, where direct length measurements are not possible, too.

A prominent astronomical scheme for moderate distance measurements is to quantify the apparent brightness (or energy flux)  $b$  of a star and compare it to its actual luminosity  $L$ , which can be derived from spectral properties. As the star has the directional characteristic of a point source, its apparent brightness  $b$  on the curved surface is inversely proportional to the adjusted circumference  $C$  of a circle with the star in its centre (see Fig. 1 for the functional dependence on the radius). We suppose an initial correlation length that is smaller than the imaging system's resolution limit so that the mutual intensity of the source can be approximated by a delta distribution<sup>27</sup>, which turns out to be formally equivalent to taking the limit  $\rho_0 \rightarrow 0$  in equations (4) and (5). If we define an effective distance based on luminosity measurements  $d_{\text{eff}} \equiv L/2\pi b = C/2\pi$  and express on its basis the correlation length  $\rho(d_{\text{eff}})$ , we qualitatively resurrect equation (1). Remarkably, the intrinsic curvature is not traceable in this set-up.

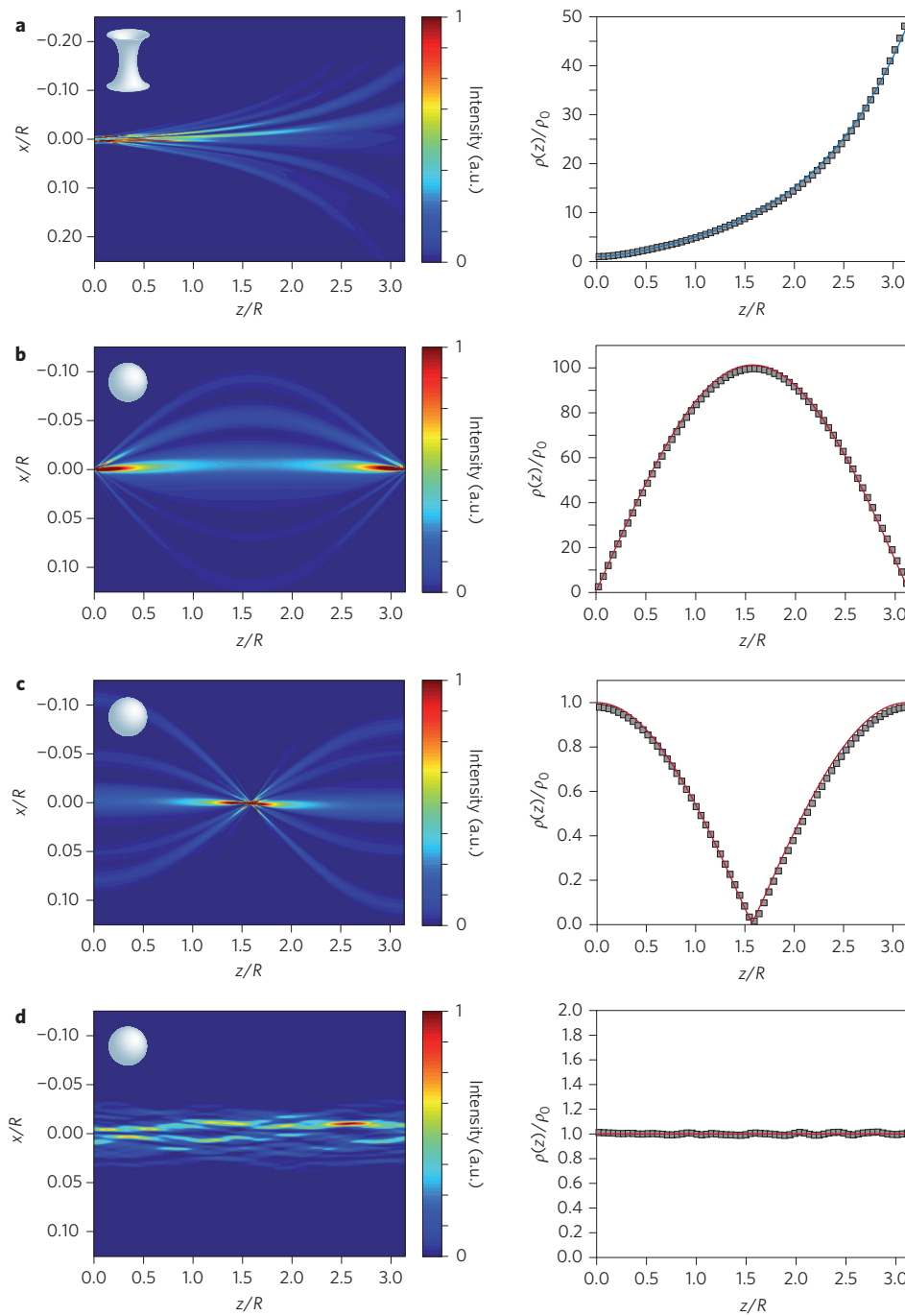


**Figure 4 | Simulations of speckle evolution on curved surfaces.** The field propagates along the figures' equators ( $t = 0$ ) with  $R = R_0 = 10$  mm and propagation constant  $k = 10^4$  mm $^{-1}$ . The ratio  $\rho_0/w_0$  is kept constant for all cases. Sample realizations are depicted on the left and the evolution of the transverse correlation length  $\rho(z)$  on the right, which in each case was derived from 1,000 phase realizations. **a**, Negatively curved surface ( $K < 0$ ) with  $\rho_0 = 0.5 \cdot \rho_{\text{stat}}$ . The blue line in the right subfigure is a plot of equation (4). **b,c,d**, Positively curved surface ( $K > 0$ ) with **(b)** short speckle diffraction length ( $z_s < R$ ),  $\rho_0 = 0.1 \cdot \rho_{\text{stat}}$ , **(c)** long speckle diffraction length ( $z_s > R$ ),  $\rho_0 = 10 \cdot \rho_{\text{stat}}$  and **(d)** the static case ( $z_s = R$ ),  $w_0 = \sqrt{2} \cdot 100$   $\mu\text{m}$  and  $\rho_0 = \rho_{\text{stat}} = 14$   $\mu\text{m}$ . The red lines are plots of equation (5).

To probe space curvature itself with this scheme, a source with finite  $\rho_0$  is required. In regard to  $d_{\text{eff}}$  we can then deduce the Gaussian curvature  $K$  from equations (4) and (5) by

$$\rho(d_{\text{eff}}) = \rho_0 \sqrt{1 + \left(\frac{1}{z_s^2} - K\right) d_{\text{eff}}^2} \quad (6)$$

which notably applies for the positively and negatively curved

and flat situation. In fact, this is a special case of a more universal strategy to retrieve  $K$  from the comparison of two different sources with varying initial parameters, the absolute distance of which to the observer is unknown apart from them being equally far away. Comparing different sets of correlation length measurements such as the ones depicted in Fig. 3 we were able to reconstruct without explicit knowledge of  $z$  the experimental surfaces' radii of curvature to be  $R_{\text{exp},K>0} = 12.8$  mm  $\pm$  0.1 mm and  $R_{\text{exp},K<0} = 14.1$  mm  $\pm$  1.1 mm, which is in very good agreement with

the actual values  $R_{K>0} = 12.5$  mm and  $R_{K<0} = 13.5$  mm, respectively (see Supplementary Material).

An astrophysical analogue to the modulated laser in our experiment might be found in extragalactic masers, which can have enormous luminosities<sup>28</sup>. Their light crosses extremely large distances and supposedly significant fractions of the universe's radius of curvature. Independent of the number of dimensions, spaces of constant curvature are uniquely determined by their so-called scalar curvature corresponding to the Gaussian curvature in two dimensions. Our 2D surfaces represent a subspace of constantly curved 4D spacetime. Hence, we anticipate that our results cover the essential dynamics of respective measurements in astronomy. Curvature effects need to be included in a constantly curved universe to extract the proper size of distant light sources from experimental data. In return, interference measurements might provide a new tool to probe spacetime curvature itself.

## Methods

Methods and any associated references are available in the [online version of the paper](#).

Received 12 June 2015; accepted 5 November 2015;  
published online 21 December 2015

## References

1. Hanbury Brown, R. & Twiss, R. Q. Correlation between photons in two coherent beams of light. *Nature* **177**, 27–29 (1956).
2. Hanbury Brown, R. & Twiss, R. Q. A test of a new type of interstellar interferometer on Sirius. *Nature* **178**, 1046–1048 (1956).
3. Hanbury Brown, R., Davis, J. & Allen, L. R. The angular diameters of 32 stars. *Mon. Not. R. Astron. Soc.* **167**, 121–136 (1974).
4. Purcell, E. M. The question of correlation between photons in coherent light rays. *Nature* **178**, 1449–1450 (1956).
5. Glauber, R. J. Photon correlations. *Phys. Rev. Lett.* **10**, 84–86 (1963).
6. Glauber, R. J. Coherent and incoherent states of the radiation field. *Phys. Rev.* **131**, 2766–2788 (1963).
7. Foellmi, C. Intensity interferometry and the second-order correlation function  $g^{(2)}$  in astrophysics. *Astron. Astrophys.* **507**, 1719–1727 (2009).
8. Malvimat, V., Wucknitz, O. & Saha, P. Intensity interferometry with more than two detectors? *Mon. Not. R. Astron. Soc.* **437**, 798–803 (2014).
9. Altman, E., Demler, E. & Lukin, M. D. Probing many-body states of ultracold atoms via noise correlations. *Phys. Rev. A* **70**, 013603 (2004).
10. Schellekens, M. et al. Hanbury Brown Twiss effect for ultracold quantum gases. *Science* **310**, 648–651 (2005).
11. Fölling, S. et al. Spatial quantum noise interferometry in expanding ultracold atom clouds. *Nature* **434**, 481–484 (2005).
12. Perrin, A. et al. Hanbury Brown and Twiss correlations across the Bose-Einstein condensation threshold. *Nature Phys.* **8**, 195–198 (2012).
13. Boal, D. H., Gelbke, C.-K. & Jennings, B. K. Intensity interferometry in subatomic physics. *Rev. Mod. Phys.* **62**, 553–602 (1990).
14. Adams, J. et al. Azimuthally sensitive Hanbury Brown-Twiss interferometry in Au+Au collisions at  $\sqrt{s_{NN}} = 200$  GeV. *Phys. Rev. Lett.* **93**, 012301 (2004).
15. Müller, B., Schukraft, J. & Wyslouch, B. First results from Pb+Pb collisions at the LHC. *Annu. Rev. Nucl. Part. Sci.* **62**, 361–386 (2012).
16. Bromberg, Y., Lahini, Y., Small, E. & Silberberg, Y. Hanbury Brown and Twiss interferometry with interacting photons. *Nature Photon.* **4**, 721–726 (2010).
17. Batz, S. & Peschel, U. Linear and nonlinear optics in curved space. *Phys. Rev. A* **78**, 043821 (2008).
18. Schultheiss, V. H. et al. Optics in curved space. *Phys. Rev. Lett.* **105**, 143901 (2010).
19. Genov, D. A., Zhang, S. & Zhang, X. Mimicking celestial mechanics in metamaterials. *Nature Phys.* **5**, 687–692 (2009).
20. Danner, A. J., Tyc, T. & Leonhardt, U. Controlling birefringence in dielectrics. *Nature Photon.* **5**, 357–359 (2011).
21. Sheng, C., Liu, H., Wang, Y., Zhu, S. N. & Genov, D. A. Trapping light by mimicking gravitational lensing. *Nature Photon.* **7**, 902–906 (2013).
22. Xu, L. & Chen, H. Conformal transformation optics. *Nature Photon.* **9**, 15–23 (2015).
23. Saleh, B. E. A. & Teich, M. C. *Fundamentals of Photonics* (Wiley, 1991).
24. Foley, J. T. & Zubairy, M. S. The directionality of Gaussian Schell-model beams. *Opt. Commun.* **26**, 297–300 (1978).
25. Friberg, A. T. & Sudol, R. J. Propagation parameters of Gaussian Schell-model beams. *Opt. Commun.* **41**, 383–387 (1982).
26. Leonhardt, U. Perfect imaging without negative refraction. *New J. Phys.* **11**, 093040 (2009).
27. Goodman, J. W. *Statistical Optics* (Wiley, 2000).
28. Lo, K. Y. Mega-masers and galaxies. *Annu. Rev. Astron. Astrophys.* **43**, 625–676 (2005).

## Acknowledgements

The authors would like to express their gratitude to R. Keding and P. Schrehardt at the glass workshop of the Max Planck Institute for the Science of Light (Erlangen) for their expertise in glass working. We are also grateful to T. Pertsch and F. Eilenberger from the University of Jena for providing a phase modulator. We gratefully acknowledge financial support by Deutsche Forschungsgemeinschaft (DFG) in the frame work of project PE 523/10-1 and the Cluster of Excellence Engineering of Advanced Materials (EAM).

## Author contributions

V.H.S. and S.B. derived the theory, V.H.S. and U.P. conceived and designed the experiments, V.H.S. performed the experiments and analysed the data, S.B. provided the MATLAB code for the simulations, V.H.S., S.B. and U.P. co-wrote the paper.

## Additional information

Supplementary information is available in the [online version](#) of the paper. Reprints and permissions information is available online at [www.nature.com/reprints](http://www.nature.com/reprints). Correspondence and requests for materials should be addressed to U.P.

## Competing financial interests

The authors declare no competing financial interests.

## Methods

In the case of normally distributed (and certain other<sup>29,30</sup>) random complex fields, the second-order DOC function of equation (2) is related to the first order DOC function through

$$g^{(2)}(x_1, x_2) = 1 + \left| \frac{\langle E(x_1)E^*(x_2) \rangle}{\sqrt{\langle |E(x_1)|^2 \rangle} \sqrt{\langle |E(x_2)|^2 \rangle}} \right|^2$$

where  $E$  is the electric field and the asterisk stands for the complex conjugate. This identity is a consequence of the complex Gaussian moment theorem and is essential for the justification of HBT-type measurements. By measuring the correlation of intensities  $I$  we gain knowledge of the modulus of the correlation of the field  $E$  and, therefore, size information of the emitting light source, as the first order DOC function is linked to the Fourier transform of the object's intensity distribution for uncorrelated light through the Van Cittert-Zernike theorem<sup>27</sup>.

All experiments were conducted with a continuous-wave laser at  $\lambda = 532$  nm and TE-polarized light. The figures were made from N-BK7 glass. The hourglass-type figure was coarsely turned with a computer controlled diamond tip and subsequently eroded and polished precisely by hand with the help of a profile template. It possesses a constant negative Gaussian curvature of  $K = -0.55 \text{ cm}^{-2}$ . A refractive index step was introduced along the surface by means of ion diffusion. By depositing the glass figure in a hot  $\text{KNO}_3$  melt the  $\text{Na}^+$ -ions of the glass close to the surface were replaced by slightly bigger  $\text{K}^+$ -ions following a diffusion law distribution. The defects in the glass structure lead to a small increase of the refractive index. The process was optimized to create a single mode waveguide for  $\lambda = 1550$  nm so that four guiding TE modes exist at the working wavelength. However, as these modes do not interfere and their effective refractive indices are very close to each other ( $\Delta n_{\text{eff}} = 8 \cdot 10^{-3}$  compared to  $n_{\text{eff}} = 1.53$ ), the Gaussian curvature  $K$  clearly dominates the dynamic of the detected intensity distribution and no deviations from single-mode excitation above the experimental resolution limit are to be expected, as was confirmed by simulations (see Supplementary Information). Reflections at the end facet make up a negligible fraction of the intensity and are pointing to the side, hence, superimposing only a small region of the primary beam. As the correlation length is ever increasing in the reflected beam, the original correlation length in the primary beam is not strongly affected by interference with field components possessing larger correlation lengths.

The solid half sphere's radius is  $R_0 = 12.5$  mm, which corresponds to a constant positive Gaussian curvature of  $K = +0.64 \text{ cm}^{-2}$ . No additional handling was necessary, as total internal reflection already ensures light propagation close to the

surface. The excitation of multiple radial modes can be treated the same way as for the waveguide structure and was shown to be negligible within the experimental resolution limit (see Supplementary Information). Back reflections at the end facet were prohibited by outcoupling of the guided light and steering it to a beam dump.

A computer-controlled transparent linear-array spatial light modulator (SLM) with a pixel size of  $100 \mu\text{m}$  was used to introduce normally distributed and finitely correlated phase shifts to an elliptically shaped laser beam of Gaussian intensity profile. The field distribution at the exit of the SLM was then imaged by a combination of elliptic lenses to the coupling facet of the glass figures. In the case of the hourglass-type figure incoupling was aided by a small coupling prism, which was attached to the front face and optically joined by drop of immersion liquid. The magnification factor of the SLM image in the transverse direction was  $M = 0.15$  for the negatively curved surface and  $M = 0.003$  to  $M = 1$  for the half spheres to implement different speckle diffraction lengths. As light propagates along the surface small defects in the otherwise smooth interface cause a small part to be scattered out of the waveguide. A CCD camera was rotated around the figures to capture images of the stray light at steps of two degrees. The images were then composed to a single panorama as shown in Fig. 3a,d,g. Perspective distortions due to the camera's point of view were compensated in MATLAB, where all evaluation took place. This procedure was repeated for 300–360 phase realizations.

For the measurements on the hourglass figure a propagation direction was chosen with a good trade-off between propagation length, spreading of the correlation length and remaining stray light intensity. As rotation symmetry holds for surfaces of constant Gaussian curvature, the proper  $x$  and  $z$  directions as used in the theory could easily be identified and the intensity profiles extracted. Only the central region of the beam (as indicated by the framing white lines in Fig. 3a,d,g) with high average intensity was considered to ensure a good signal-to-noise ratio in the camera. As the speckle patterns are only slowly varying in the propagation direction, the intensity profiles were averaged over four propagation steps about  $100 \mu\text{m}$  apart to reduce noise originating from stray centres.

The simulations were conducted by means of (1+1)-dimensional beam propagation method (BPM). The initial fields were generated to be spatially correlated and normally distributed in their real and imaginary parts independently.

## References

29. Reed, I. S. On a moment theorem for complex Gaussian processes. *IRE Trans. Inform. Theor.* **8**, 194–195 (1962).
30. Picinbono, B. & Boileau, E. Higher-order coherence functions of optical fields and phase fluctuations. *J. Opt. Soc. Am.* **58**, 784–789 (1968).